PAPER

Ligand-based design, molecular dynamics and ADMET studies of suggested SARS-CoV-2 Mpro inhibitors

Nada M. Mohamed, [ID] *[a] Eslam M. H. Ali[ab] and Asmaa M. AboulMagd [ID] [c]

Severe Acute Respiratory Syndrome Coronavirus 2 (SARS-CoV-2) has been the choice of recent studies worldwide to control its pandemic. Given the similarity with the earlier SARS-CoV, it is possible to use the previously reported inhibitors to develop a new treatment for the current attack of SARS-CoV-2. This study used the formerly published SARS-CoV Mpro small-molecule protease inhibitors to develop a pharmacophore model in order to design new ligands. Several strategies and scaffolds were evaluated *in silico* giving rise to ten newly designed compounds. Molecular docking and dynamics simulations were performed on Mpro enzyme in its active site to evaluate the newly designed ligands I–X. The results obtained from this work showed that compounds III–VI had a better molecular docking score than the co-crystallized ligand baicalein (3WL) giving -5.99, -5.94, -6.31, -6.56 and -5.74 kcal mol^{-1}, respectively. Moreover, they could bind to the Mpro binding site better than I, II and VII–X. The most promising chromen-2-one based compounds V–VI had sufficiently acceptable physicochemical and ADMET properties to be considered new leads for further investigations. This new understanding should help to improve predictions of the impact of new treatments on COVID-19.

1. Introduction

The World Health Organization (WHO) announced the pandemic alert for Severe Acute Respiratory Syndrome Coronavirus 2 (SARS-CoV-2) in March 2020. The newly-discovered virus has over 40 million confirmed cases worldwide including over one million deaths as reported by the WHO in October 2020 and the numbers are still rising.[1] Since then, many researchers have been studying its phylogenic similarity with other *Coronaviridae* family members in order to find or design a suitable treatment. Scientists found that SARS-CoV-2 was ~80% similar to SARS-CoV in its primary structure, however there are some differences in the occurrence of the accessory proteins.[2,3] Both SARS viruses use the human angiotensin II receptor (ACE-II) as their port to conquer the human cell and control its machinery. Several studies have been undertaken to meet the need to find a suitable treatment for SARS-CoV-2 symptoms and control its complications. To the date of commencing this study, no small molecule drug has been approved for SARS-CoV-2 treatment, however, only remdesivir (ribonucleotide analogue inhibitor of viral RNA-dependent RNA polymerase) has been approved by the Food and Drug Administration (FDA) for emergency use in hospitalized patients.[4,5]

The *Coronaviridae* family shared the positive-sense single stranded RNA genome but with variable sizes between 26–32 Kb. This genome encoded 4 structural (spike, envelop, membrane and nucleocapsid), 15 non-structural proteins (nsps) one of which is nsp5 that encodes chymotrypsin-like cysteine major protease enzyme (Mpro) and 8 accessory proteins as presented in Fig. 1.[6,7] The Mpro is found to be a crucial enzyme in the viral gene expression and replication. This enzyme is responsible for the major proteolysis of the large polyproteins 1a (PP$_{1a}$) and 1b (PP$_{1b}$) to yield many functional proteins like RNA-dependent RNA polymerase. Consequently, inhibiting Mpro stopped the viral replication inside the host cell.[8,9]

Unlike other cysteine and serine proteases; Mpro has only two residues forming the catalytic dyad (His 41 and Cys 145) and one molecule of water located close to His 41 which supposedly acts as the third residue for its catalytic activity.[10,11] The proteolytic mechanism of Mpro involves several steps initiated by the imidazole ring of His 41 deprotonates the sulfhydryl group of Cys 145. Then the resulting nucleophilic thiolate ion attacks the peptide linkage of the viral polyproteins at 11 different sites with the recognition sequence of Leu-Gln↓-(Ser/Ala/Gly) (↓ meant the cleavage site) as explained in Fig. 2.[12,13]

Structurally, Mpro enzyme is a homodimer in which each monomer is almost perpendicular on one another and its monomeric form is enzymatically inactive.[14] Each monomer

[a]Pharmaceutical Chemistry Department, Faculty of Pharmacy, Modern University for Technology and Information (MTI), Egypt. E-mail: nada.mostafa@pharm.mti.edu.eg
[b]University of Science & Technology (UST), Yuseong-gu, Daejeon, 34113, Republic of Korea
[c]Pharmaceutical Chemistry Department, Faculty of Pharmacy, Nahda University (NUB), Beni-Suef, Egypt
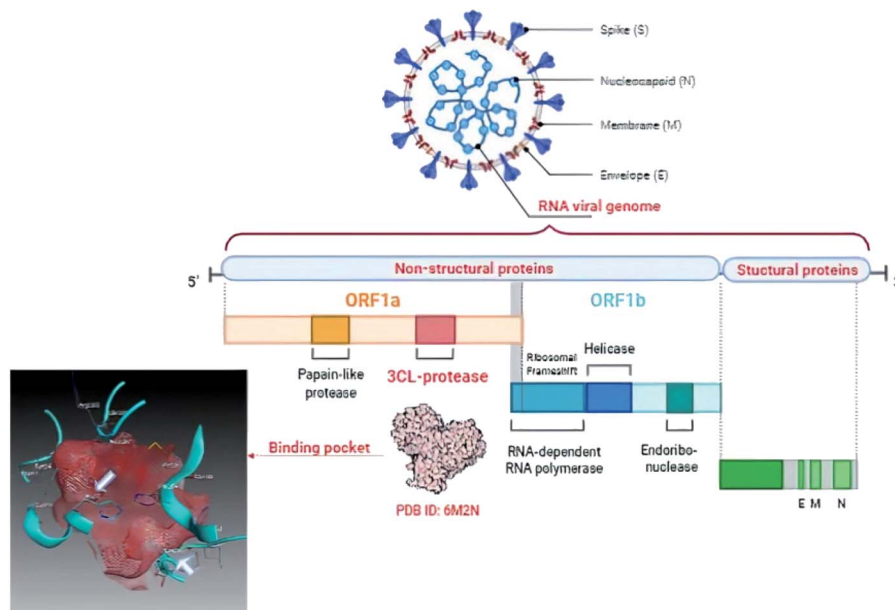
Fig. 1 Graphical presentation of SARS-CoV-2 viral composition showing the binding pocket of M^{pro} where the white arrows pointed to the catalytic dyad.

consists of three main domains involving the amino acid residues 1–101, 102–184 and 201–301, respectively. Considering their spatial conformation; the first two domains are in the form of antiparallel β-barrel while the third is formed of five α-helices where the substrate binding site is located at the cleft between the first two domains as shown in Fig. 3.[15] The substrate binding site consists of three main regions namely; catalytic dyad, deeply buried subunits S1, S2 and shallow buried subunits S3–S5. The catalytic dyad that is responsible for the proteolytic activity of the M^{pro} which is formed of His 41 as proton acceptor and Cys 145 as the nucleophile as explained

earlier. The deeply buried subunits S1 and S2 are the main site for hydrophobic and electrostatic interaction between M^{pro} and the substrate or the inhibitor agent. It consists of His 163, Glu 166, Cys 145, Gly 143, His 172, Phe 140 and Cys 145, His 41, Thr 25 as S1 and S2, respectively. On the other hand, the shallow subunits S3–S5 are formed from Met 165, Glu 166, Gln 189, Met 49 and His 41.[16] The dimerization formed by the interaction of the N-terminus of one monomer with Glu 166 of the other is crucial to keep the correct conformation of the substrate binding pocket in S1 subunit.[13,17] Therefore, if an agent could bind to the catalytic dyad, dimerization essential amino acids or
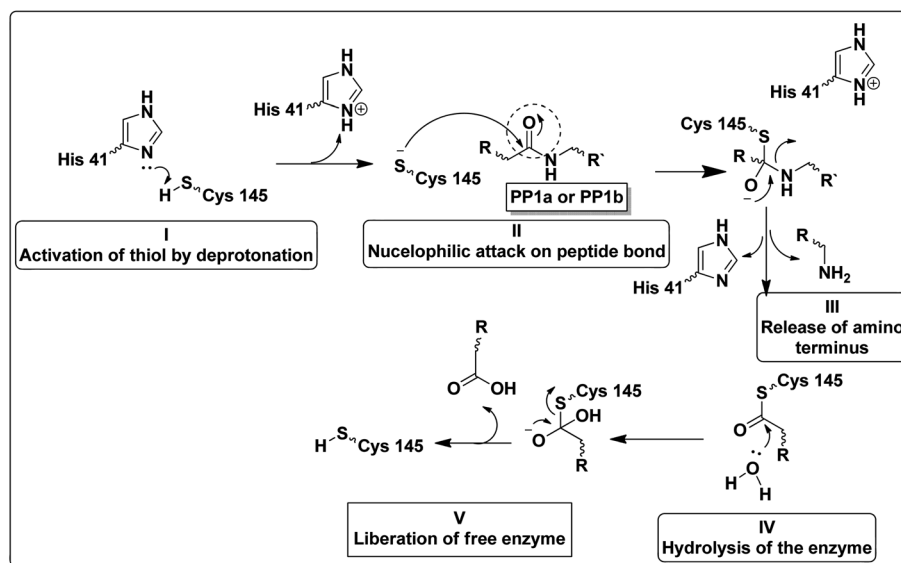

Fig. 2 Steps of the proteolytic mechanism of SARS-CoV-2 M^{pro} enzyme.[12,13]
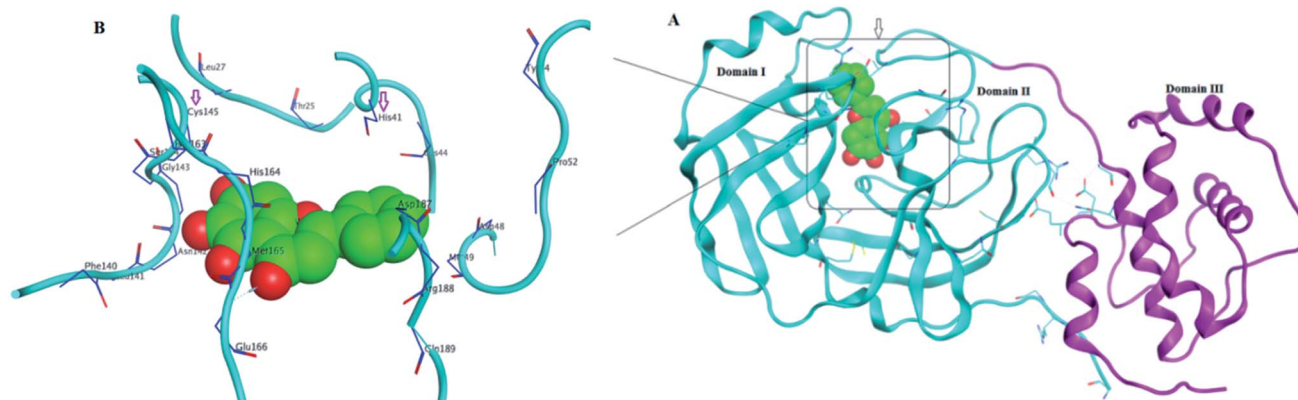
Fig. 3 SARS-CoV-2 M^{pro} protein structure (PDB: 6M2N) where (A): the full structure of the enzyme showing β-barrel of both domain I and II (blue), the helical shape of domain III (magenta) and the binding site of ligand (green spheres) (B): the binding site structure showing the ligand (green spheres) was surrounding with the crucial amino acid residues for interaction.

other residues that blocked the access of the natural substrate then it might inhibit with great possibility the proteolytic action of the enzyme and hinder the viral replication.

Recent homology studies have revealed that the structure of M^{pro} enzyme of both SARS-CoV and SARS-CoV-2 have 96% similarity in their amino acid composition. However, they differ in only 12 amino acid residues with one residue (A46S) present in the proximity of the substrate binding site and other considerable mutations of T285A and I286L. This mutation was reported to increase the SARS-CoV M^{pro} catalytic activity by 3.6 folds which might explain the observed higher proteolytic activity of SARS-CoV-2 M^{pro}.[14,18] Nonetheless; none of the 12 variant residues practically affect its enzymatic activity.[19,20] Therefore, inhibitors of SARS-CoV M^{pro} enzyme are considered the milestone in designing new inhibitors for its SARS-CoV-2 M^{pro} sibling enzyme. In addition, the human cells have no

proteases with a matching cleavage specificity of M^{pro} which offers an excellent drug target with minimal toxicity level.

Several publications had been screened for potent small molecule inhibitors of SARS-CoV-2 M^{pro} either of natural or synthetic nature. Amongst the natural ones; Sekiou et al. had reported many natural products with in silico inhibitory activity on CoV-2 M^{pro} namely; quercetin **1**, hispidulin **2**, cirsimaritin **3**, artemisin **4**, curcumin **5**, thymoquinone **6** and eugenol **7** as shown in Fig. 4.[21] It was reported that the ability of **1–7** to bind to the crucial amino acid residues of M^{pro} active site using PDB: 6LU7 with binding affinities −7.5, −7.3, −7.2, −6.8, −6.8, 5.1 and −4.9 kcal mol^{-1}, respectively. On the other hand, Yao et al. had proven in vitro the capability of baicalein **8**, a flavonoid found in traditional Chinese medicine, and its glycosylated form baicalin **9** to inhibit M^{pro} proteolytic activity with IC$_{50}$ 0.94 and 6.41 μM, respectively. Moreover, both **8** and **9** had shown free
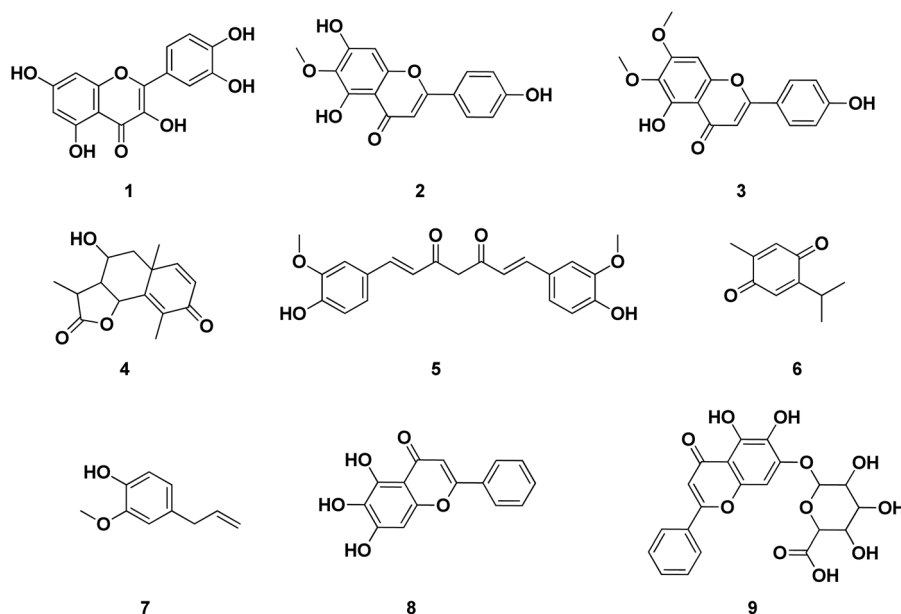

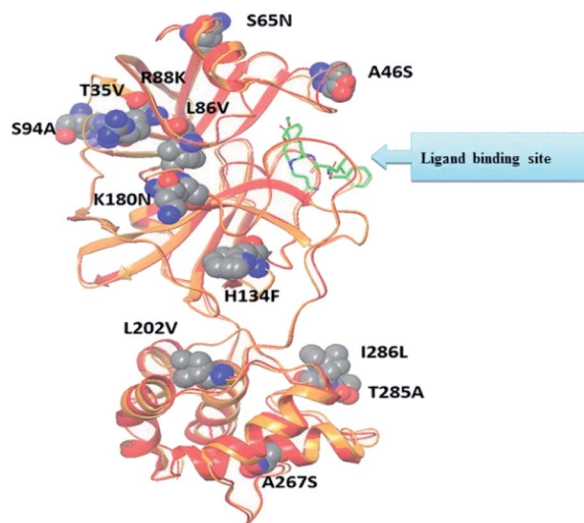**Fig. 4** Reported structures with inhibitory activities on SARS-CoV-2 M^{pro} enzyme.

Fig. 5 Alignment of SARS-CoV M^pro (PDB ID: 2A5I, red ribbon) and SARS-CoV-2's M^pro (PDB ID: 6LU7, orange ribbon) X-ray structures. As a result of pairwise alignment, sequence identity showed 96%. The green stick indicates the inhibitor binding site, and sphere model indicates residues that are not conserved between both sequences.[28]

binding affinity ΔG^{ITC} of -30.78 and -28.2 kJ mol^{-1}, respectively.[22] Compounds with chromen-4-one scaffold **1–3** and **8–9** had demonstrated remarkable inhibitory activity on SARS-CoV-2 M^pro which was used as the core of this study.

2. Rational and design

Literature review of the SARS-CoV M^pro small molecule inhibitors revealed common structural features. Almost all inhibitors have two hydrophobic centers; with one has one or more H-bond acceptor atoms, both linked with 2 to 3 H-bond acceptor/donor atoms as detailed in Fig. 5 and 6.

Consequently, pharmacophore mapping was formed to screen the newly suggested structures followed by docking on SARS-CoV-2 M^pro and molecular dynamic simulation to predict their activity.

Herein, the newly designed molecules reserved the common structural features of SARS-CoV M^pro inhibitors with modification on one of the hydrophobic centers using bioisostere rings either five- or six membered. This study focused on benzo-triazole, pyridine and coumarin scaffolds with proven inhibitory activity on SARS-CoV M^pro.[23–27] Considering the linkage atoms; other alternatives of the ester linkage were to be evaluated. In this study, amide as the ester bioisostere and guanidine linkers were evaluated as detailed in Fig. 7.

Computational techniques have long been of value in rational drug design and discovering new hits. This study focused in using ligand-based drug design theories as a source to get the required pharmacophore features to inhibit SARS-CoV-2 M^pro enzyme. Moreover, molecular dynamic simulation (MD) would be used to evaluate the interaction between the M^pro enzyme and its newly-designed inhibitors where MD studies the dynamics between the enzyme in solution with the inhibitors at the atomic level according Newton's equation of motion.[29,30]

3. Experimental methods

All *in silico* methods were conducted and visualized using MOE® 2020 (Molecular Operating Environment) software through Windows® 10 operating system.

3.1. SARS-CoV and SARS-CoV-2 M^pro alignment

As stated earlier, the binding site of both SARS-CoV and SARS-CoV-2 M^pro shared very close amino acid residues and spatial conformation therefore in this current work, protein alignment protocol was conducted at first to demonstrate both enzymes
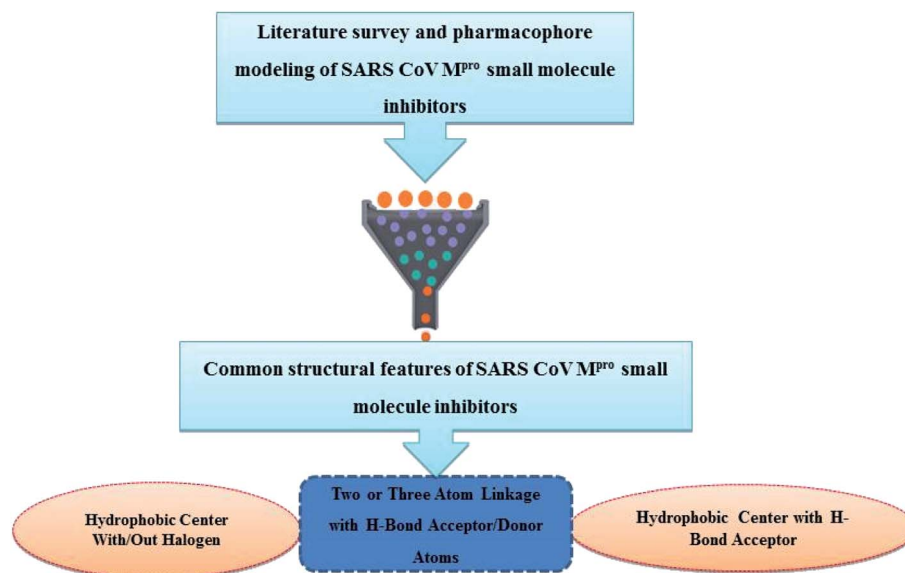

Fig. 6 Common structural features of SARS-M^pro small molecule inhibitors.
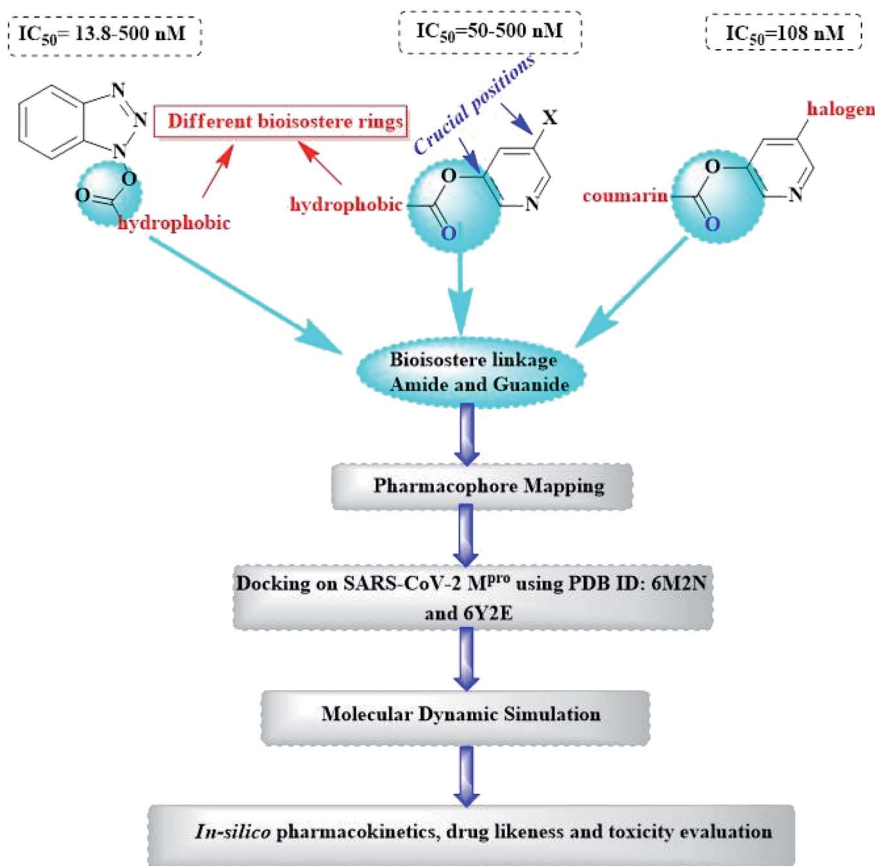
© 2021 The Author(s). Published by the Royal Society of Chemistry

Fig. 7 Design of newly suggested SARS-CoV-2 M^{pro} small molecule inhibitors.

binding sites superimposition and assess their similarity using Protein Data Bank (PDB) files 2A5K and 6M2N for SARS-CoV and SARS-COV-2 M^{pro}, respectively. This step was essential to prove that both files used for the upcoming *in silico* study were of high similarity and matched the literature.

The two crystal structures were downloaded where their energies were minimized. The protein chains were designated to unique protein unit chain tag and were subjected to flexible alignment. The superposition algorithm started with alignment of the sequences using a modified version of Needleman and Wunsch algorithm.[31] The alignment began with building up the initial pairwise similarity matrix using either a progressive or a tree-based method. Then round-robin realignment was performed, followed by a randomized iterative refinement. Finally, structure based realignment was performed using the existing or predicted protein secondary element information. After this, 3D superposition would be done on the best aligned model.

3.2. Pharmacophore modeling

3.2.1. Training set selection and conformational analysis. Training set of 43 SARS-CoV M^{pro} inhibitors with structural diversity and wide range of inhibitory activity were collected from different research papers, all compounds were built in 2D structure using ChemDraw® software, MOE® software was used

for the molecular visualization and minimization to the closest local minimum using the CHARMm-like force field.

3.2.2. Common features pharmacophore and compounds mapping. Structural information from the training set identified a set of features crucial for activity and was considered to represent a pharmacophore hypothesis. The best model generated contains two types of chemical features, namely, H-bond acceptor (HBA) and hydrophobic features. The pharmacophore query was generated using hydrogen bond acceptor (HBA), hydrophobic (H) and ring aromatic (RA) chemical features. A group of nineteen energetically reasonable conformational models was generated. The selected pharmacophore model represented by two aromatic hydrophobic centers (F1: Aro/Hyd and F2: Aro/Hyd) and one H-bond acceptor–metal ligature center (F3: ACC/ML). The top ranked pharmacophore model was used for mapping the newly designed compounds where they showed typical fitting in the pharmacophore model with RMSD values less than 1.

3.3. Molecular docking

Molecular docking was performed using MOE® 2020 and MMFF94x force field. The X-ray crystal structures of SARS-CoV-2 M^{pro} enzyme were downloaded for the Protein Data Bank (PDB: 6M2N co-crystallized with 3WL and 6Y2E as free enzyme). Before implementing the docking procedure; both protein
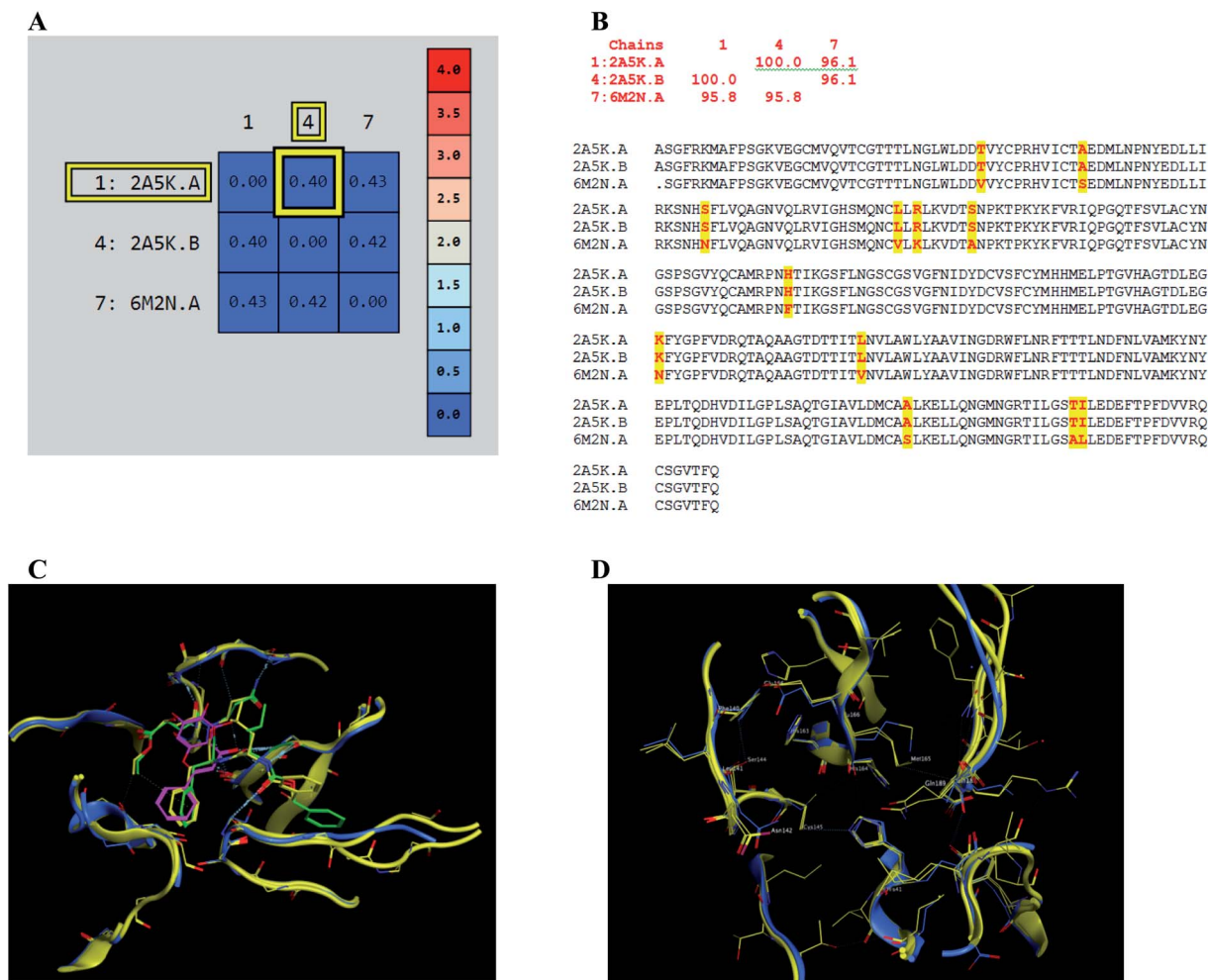
Fig. 8 Similarity of both SARS-CoV and SARS-CoV-2 M^{pro} as amino acid sequence and spatial conformation where (A) was pairwise similarity matrix, (B) was amino acid sequence of both chains of 2A5K and one chain of 6M2N with highlighted differences. (C and D) Were both pockets alignment where 2A5K chains appeared in yellow and 6M2N chain in blue with and without ligands, respectively where 3WL showed in magenta color and AZP in green.
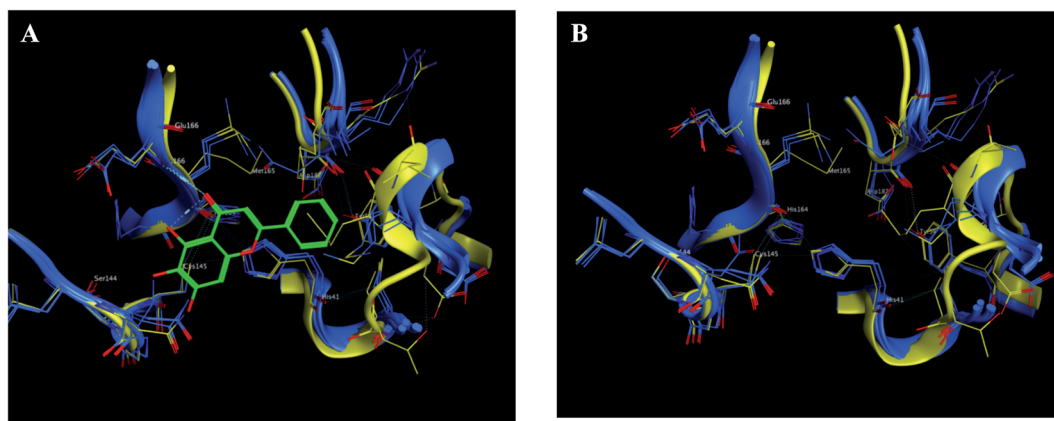

Fig. 9 The 2D representation of SARS-CoV-2 M^{pro} conformations both the free PDB: 6Y2E and the bound PDB: 6M2N. (A) and (B) Showed the conformation similarity between both PDB crystals with and without ligand 3WL, respectively where 6M2N chains appeared blue, 6Y2E chain in yellow and 3WL in green sticks.

amino acid sequences were corrected and protonated at the default pH and 293 K temperature as mentioned in the experimental section of the PDB file. Visualization and generation of the 3D figures were performed using MOE® 2020 software.

Chain a of PDB: 6M2N was selected for docking and the method was validated giving RMSD of 0.35 using triangle matcher as placement algorithm, London dG as rescoring function 1 and GBVI/WSA dG as rescoring function 2 algorithm. Similarly; the free enzyme crystal PDB: 6Y2E was docked using dummy atoms algorithm allocated to the critical interacting amino acid residues with the human ACE-II receptor using the same force field, placement and rescoring functions.
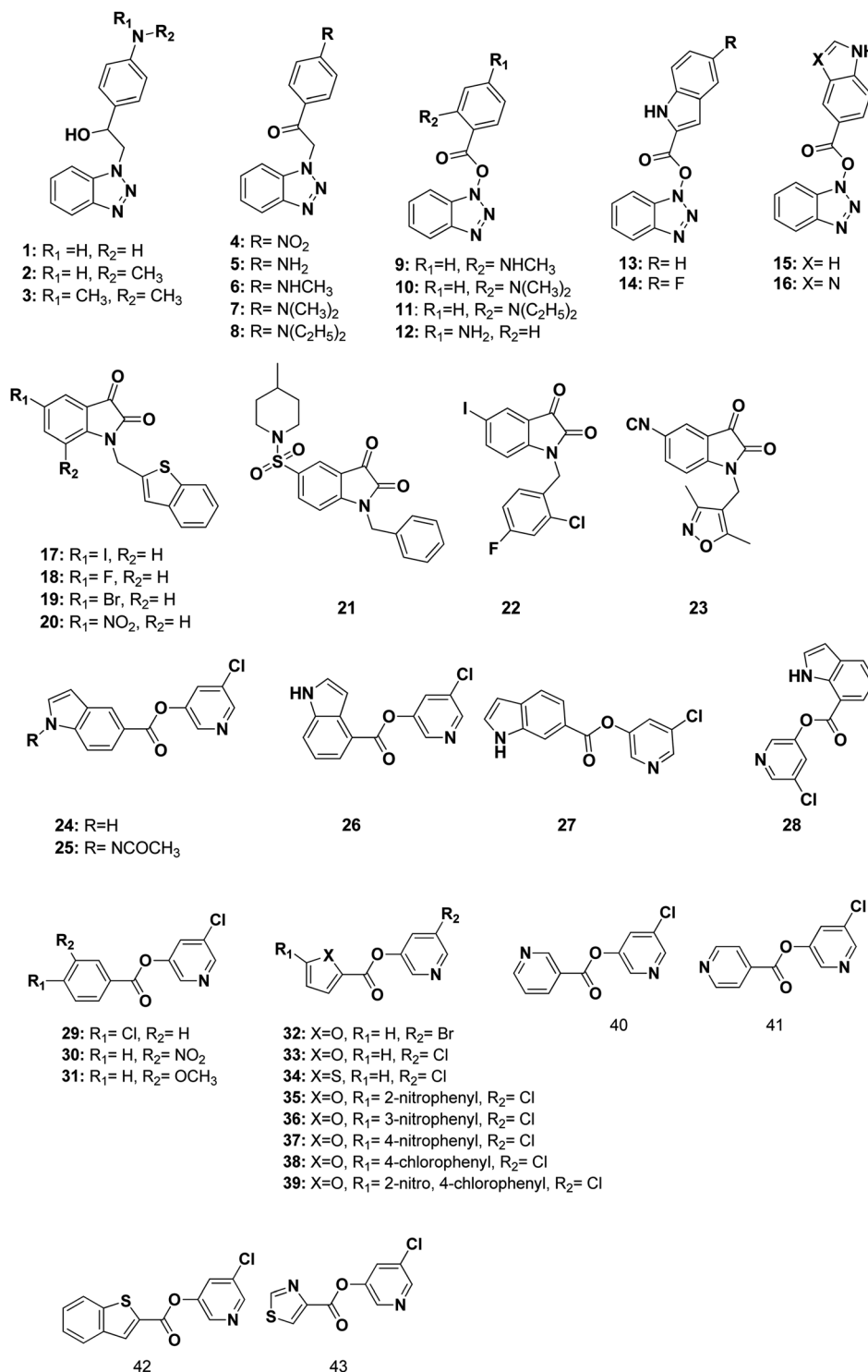

Fig. 10 Structures of the used reported small molecule SARS–CoV M^{pro} inhibitors to design the pharmacophore model.
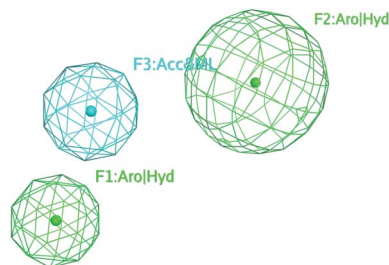
Fig. 11 The common features of the pharmacophore model generated from training set alignment of SARS–CoV M^{pro} inhibitors.

3.4. Molecular dynamics simulation

The molecular dynamics (MD) simulation study was performed for the suggested compounds to target SARS-CoV-2 M^{pro} complex (PDB: 6M2N) using standard default parameter setting in the MOE® 2020 software. There are four algorithms implemented in MOE® software for MD simulations; the Nos_e-Poincar_e-Andesen (NPA), the Nos_e-Hoover-Andersen (NHA), Berendsen velocity/position (BER) and Nanoscale Molecular Dynamics (NAMD). In this study, the NPA which is the most precise and sensitive algorithm, was used to study the molecular dynamics of ligands.[32]

During the MD calculations, the system was optimized by selecting MMFF94x force field, water as a solvent, six margins and delete far existing solvent with distance greater than 4 Å. Also, the trajectories were stored in the traj.trr file for the models and structural analysis was done at every picosecond.

4. Discussion

Establishing a full understanding of the close similarity of both amino acid sequence and structure between SARS-CoV and SARS-CoV-2 M^{pro} enabled to study several small molecule inhibitors of SARS-CoV M^{pro} to propose a pharmacophore

model which in turn would be used for developing new inhibitors for SARS-CoV-2 M^{pro}.

4.1. SARS-CoV and SARS-CoV-2 M^{pro} alignment

The presented comparison of both SARS-CoV and SARS-CoV-2 M^{pro} binding sites effectively defined the ligand molecular binding to provide useful visions into the molecular interaction pattern of the co-crystalized ligands. As demonstrated in Fig. 8a and b, a similarity of 95.8–96.1% was observed between both binding sites of SARS-CoV and SARS-CoV-2 M^{pro} where the two chains of 2A5K were identical. These achieved data complied with the reported data of high similarity between both Coronae viruses M^{pro} active sites and the fact that the majority of the dissimilarity was slightly far from the targeted site. The difference in their amino acid sequence was found to be as follow where the first letter belongs to SARS-CoV and the last belongs to SARS-CoV-2; T35V, A46S, S65N, L86V, R88K, S94A, H134F, K180N, L202V, A267C, T285A, I286L which matched the literature showing only A46S was at the vicinity of the active site without affecting its proteolytic activity.[33] Furthermore; this alignment displayed that whether the inhibitor was small molecule as 3WL or peptide – like as AZP, they should bind to the same residues to achieve a respectful inhibitory activity. Consequently, the design of small molecule SARS-CoV-2 M^{pro} inhibitors based on the previously published SARS-CoV M^{pro} enzyme inhibitors was of appreciated value during this study. The superposition of the two active sites with and without ligands illustrated a high similarity between the corresponding enzymes sequence that could clearly appear in their ligands (AZP and 3WL) high alignment as displayed in Fig. 8c and d.

4.1.1. SARS-CoV-2 free and bound M^{pro} alignment. In another aspect, the difference between the free and bound conformations of SARS-CoV-2 M^{pro} was studied to make sure that the newly-designed compounds could inhibit both conformations to get a fruitful outcome. As observed in Fig. 9, both the free
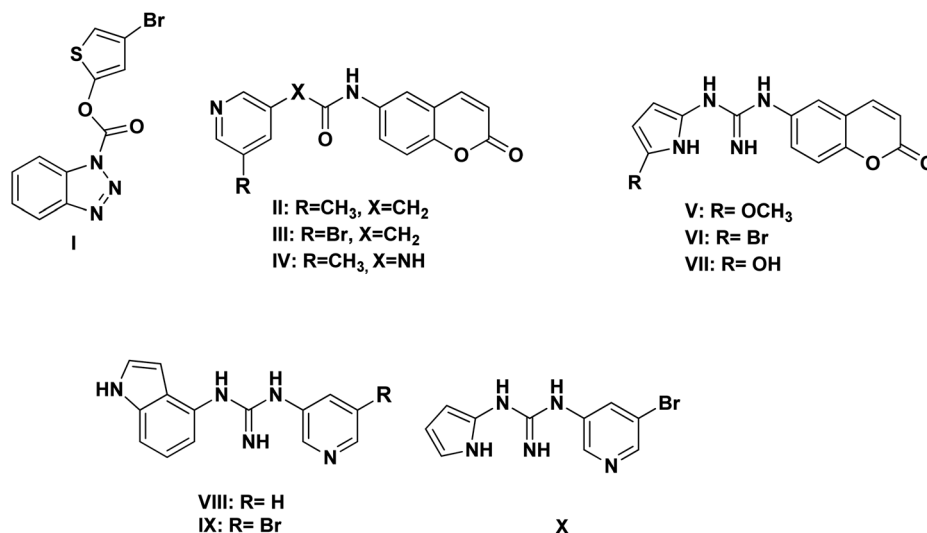

Fig. 12 Chemical structures of the newly proposed compounds I–X as SARS–CoV-2 M^{pro} inhibitors.

and bound crystals of SARS-CoV-2 M^{pro} exhibited the same conformation that was not affected by their ligand presence.

4.2. SARS-CoV M^{pro} pharmacophore model development

The 3D pharmacophore model was built using the previously reported CoV M^{pro} small molecule inhibitors which exhibited a broad range of structural variability and biological activity.[24–26,34,35] Those inhibitors training set could properly detect the essential moieties of the existing SARS-CoV M^{pro} inhibitors having the same mechanism of inhibition. Afterward, the model was used as 3D search query for predicting the structural requirements of each compound to identify SARS-CoV-2 M^{pro} new inhibitors. In this study, a training set of 43

reported SARS-CoV M^{pro} inhibitors were collected and their chemical structures are shown in Fig. 10.

The selected pharmacophore model represented by two aromatic hydrophobic centers (F1: Aro/Hyd and F2: Aro/Hyd) and one H-bond acceptor–metal ligature center (F3: ACC/ML) was shown in Fig. 11.

4.3. Structural consideration to design new SARS-CoV-2 M^{pro} inhibitors

Based on the literature survey of many active SARS-CoV M^{pro} small molecule inhibitors with benzotriazole, pyridine and coumarin scaffolds and its proven similarity with SARS-CoV-2 M^{pro}; several new compounds were proposed aiming to
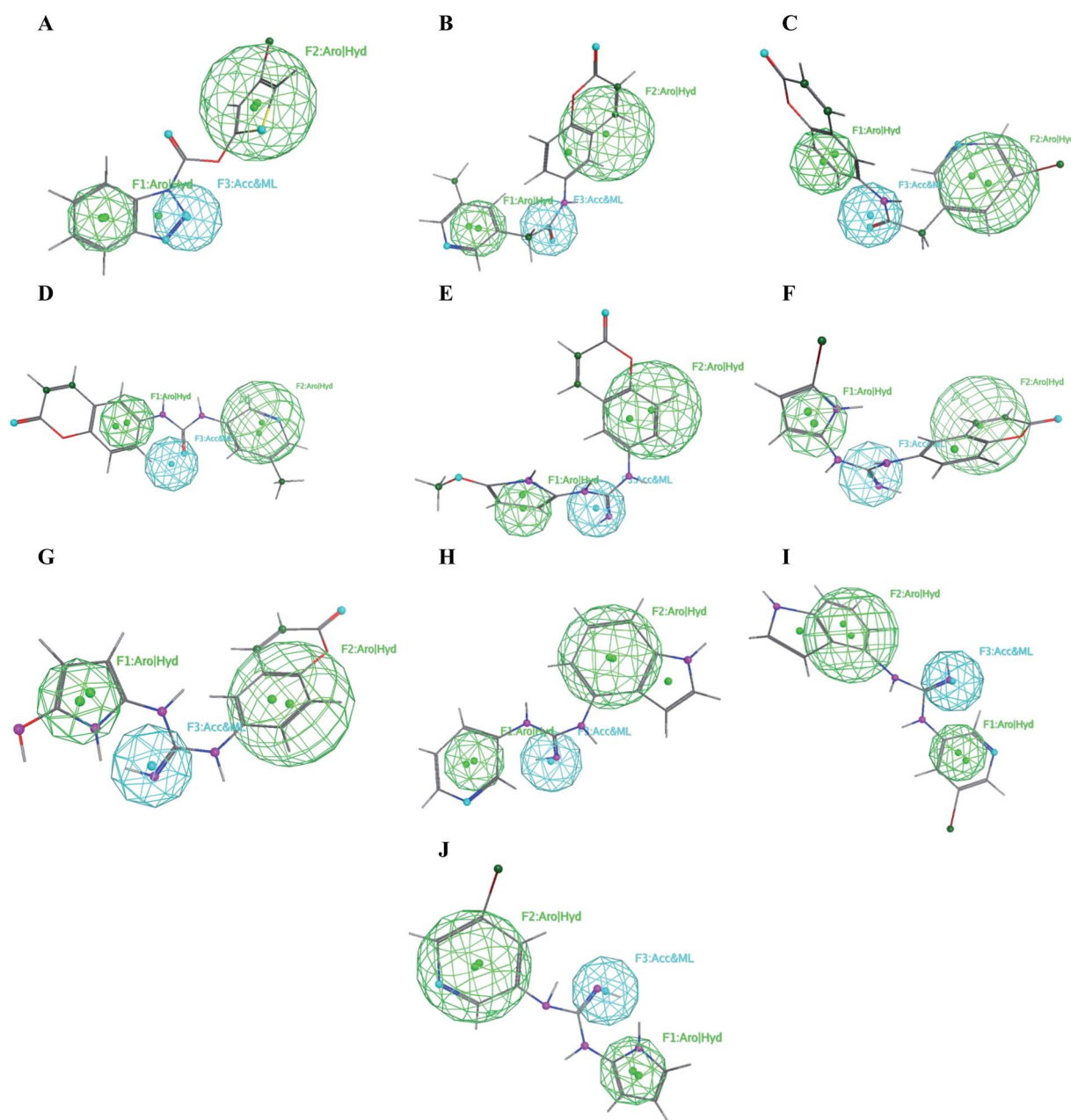

Fig. 13 Mapping of the target compounds I (A), II (B), III (C), IV (D), V (E), VI (F), VII (G), VIII (H), IX (I) and X (J) on the generated pharmacophore model.

Fig. 14 The overlaid co-crystallized ligand 3WL of SARS-CoV-2 M^{pro} (PDB: 6M2N) whilst docking method validation. (A) Shows 2D structures of the co-crystallized ligand (red) and the re-docked ligand (green) showing the interacting amino acid residues. (B) 3D visualization of overlay co-crystallized ligand (green sticks) and re-docked ligand (magenta sticks).

identify a potent lead for the current SARS-CoV-2 outbreak control. Designing these new compounds considered the previously discussed structural considerations which in turn were submitted for pharmacophore mapping and molecular docking to choose the best lead. Compounds **I–X** showed in Fig. 12 were the best regarding their pharmacophore RMSD and molecular docking binding energy score as detailed later.

Fig. 15 Crucial amino acids 2D interaction between SARS-CoV-2 M^{pro} (PDB: 6M2N) and the proposed compounds **II–VI** where (A) is for **II**, (B) for **III**, (C) for **IV**, (D) for **V** and (E) for **VI**.

Table 1 Pharmacophore mapping and docking results of the proposed compounds as relevant to 3WL. The essential amino acid residues interacting with the compounds are shown in bold

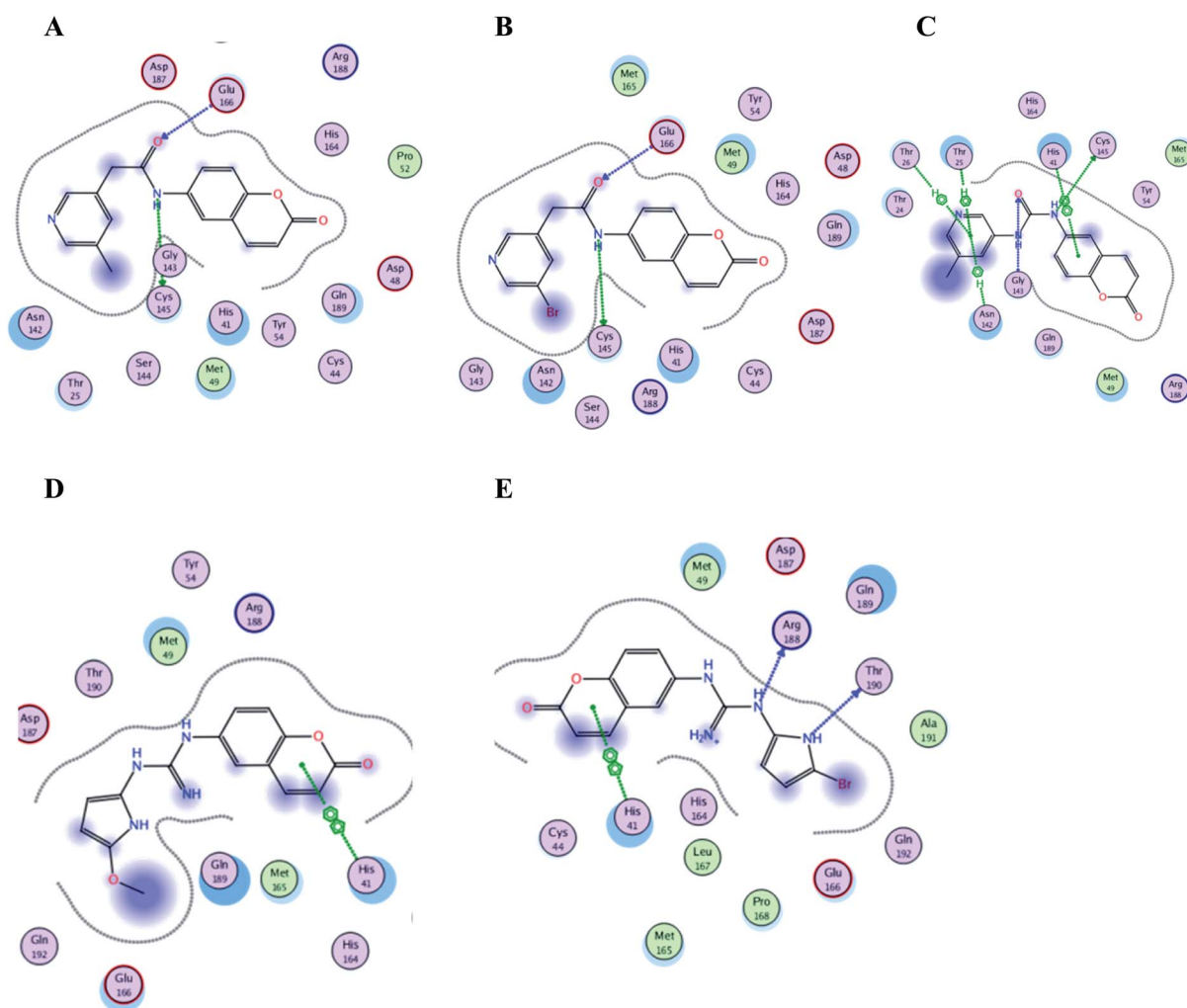| # | Pharmacophore RMSD | Docking using 6M2N | | | Docking using 6Y2E | | |
		Score (kcal mol^{-1})	No. of interacting residues	Interacting residues	Score	No. of interacting residues	Interacting residues
3WL	NA^a	−5.77	2	**Glu 166, His 163**	−4.66	2	**Cys 145, Glu 166**
VI	0.57	−6.56	3	**His 41**, Arg188, Thr 190	−5.16	2	**His 41, Cys 145**
V	0.43	−6.31	1	**His 41**	−5.69	2	**Cys 145**, Asn 142
III	0.65	−5.99	2	**Cys 145, Glu 166**	−5.73	1	**Cys 145**
IV	0.70	−5.94	6	**His 41, Cys 145**, Gly 143, Asn 142, Thr 25, Thr 26	−5.66	5	**His 41, Glu 166**, Asn 142, Met 49
II	0.21	−5.82	2	**Cys 145, Glu 166**	−5.72	2	**His 41, Cys 145**
VII	0.52	−5.75	1	**Cys 145**	−5.68	2	Thr 26, Asn 142
I	0.20	−5.64	1	**His 41**	−5.16	3	**His 41, Cys 145**, Asn 142
V	0.67	−5.49	2	Thr 26, Asn 142	−5.50	1	Met 165
VI	0.58	−5.33	2	**His 41**, Gly 143	−5.01	1	**Glu 166**
IV	0.54	−5.25	3	Asn 142, Thr 25, **Cys 145**	−5.27	1	Met 165

^{a} NA is not available.

Upon screening the best benzotriazole structural features; Wu *et al.* mentioned that the position of the ester linkage was critical *versus* the nitrogen and was superior to ether, carbonyl or methylene linkage.[24,26] Moreover, the importance of adding a halogen group to the *meta* position of the other aromatic ring was described.

Considering the other reported SARS-CoV M^{pro} inhibitors with pyridine center; the published data stated the importance of adding a halogen atom to the *meta* position of the pyridine ring which was linked to the other hydrophobic center at the other *meta* position. Interestingly, adding bromide group to the pyridine ring was superior to chloride. Furthermore, changing the ester linkage with an amide abolished their inhibitory activity which was considered during the design of the new compounds **VIII–X** using guanidine linkage instead.[25,34]

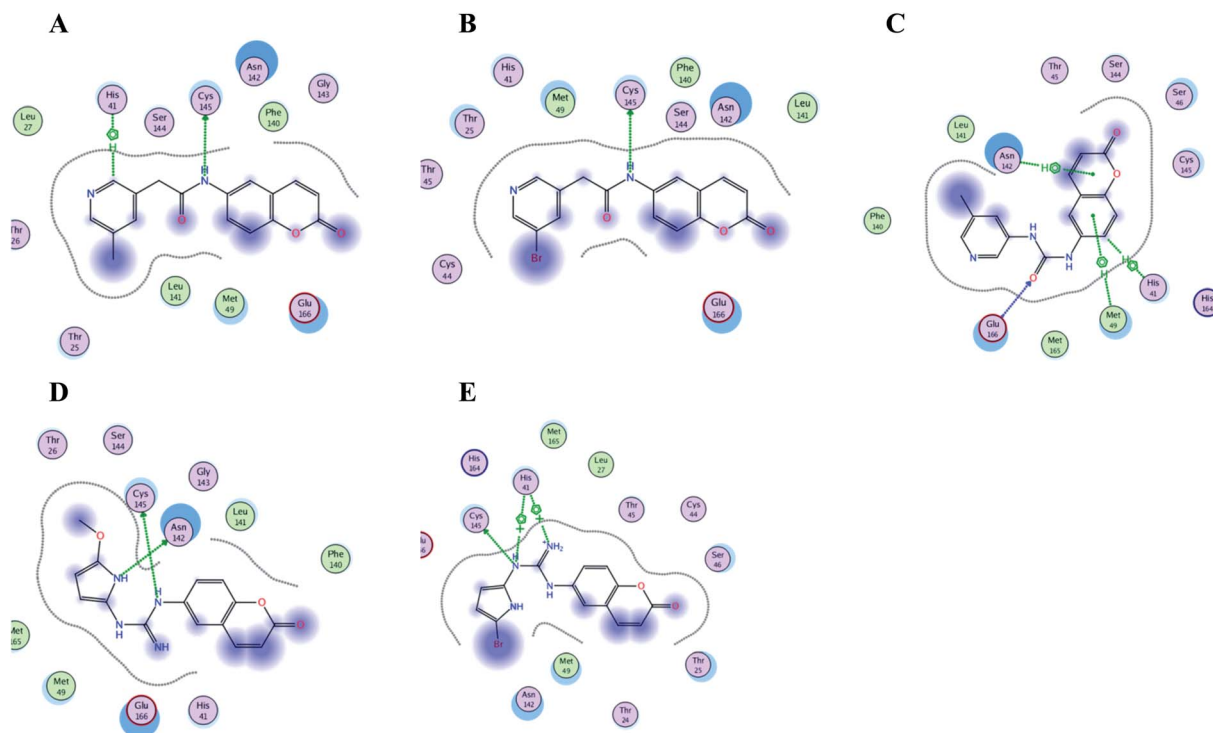

Fig. 16 Crucial amino acids 2D interaction between SARS-CoV-2 M^{pro} (PDB: 6Y2E) and the proposed compounds **II–VI** where (A) is for **II**, (B) for **III**, (C) for **IV**, (D) for **V** and (E) for **VI**.

Paper

4.4. Pharmacophore mapping

The obtained data illustrated the high affinity of the tested compounds **I–X** in the selected pharmacophore model with RMSD values less than one. Hence; they all preserved the main structural features generated in the pharmacophore model as shown in Fig. 13.

It was observed that compounds **II–IV** fitted the model where the H-bond acceptor–metal ligature center was characterized by the acetamide or urea moieties and both pyridine and chromen rings represented the required aromatic hydrophobic centers F1 and F2-Aro/Hyd, respectively. In a quite similar manner, **V–X** showed similar pharmacophore fitting behavior where the central guanidine moiety represented the H-bond acceptor–metal ligature center, while the lateral aromatic rings represented the two aromatic hydrophobic centers F1 and F2-Aro/Hyd, respectively. However; compound **I** behaved differently, the H-bond acceptor–metal ligature center was represented by the three nitrogen atoms of the triazole ring. In the mean while the terminal thiophen ring indicated one of the aromatic hydrophobic centers and the other center represented by the phenyl part of benzo[*d*][1,2,3]triazole moiety as declared in Fig. 13a.

4.5. Molecular docking

In order to get a reliable docking result; two X-ray crystals namely, PDB: 6M2N and 6Y2E were used to computationally evaluate the proposed compounds **I–X** binding energies and their interactions with the crucial amino acids inside SARS-CoV-2 M^{pro} binding site. Consequently; to validate the used docking method using PDB: 6M2N the cocrystallized ligand baicalein **8** (3WL) was redocked using several docking protocols and algorithms untill reaching RMSD 0.35 and close 3D alignment as showed in Fig. 14. Meanwhile docking using dummies allocated by MOE® site finder algorithm showing the crucial amino acids was used while docking using PDB: 6Y2E.

Interestingly; all the ten proposed compounds showed either better energy score or number of interaction with the crucial residues than 3WL as summarized in Table 1 and presented in Fig. 15 and 16. The co-crystallized ligand 3WL was docked to 6Y2E as a reference to assess **I–X** using same docking protocol.

It was reported that baicalein **8** (3WL) demonstrated 99.4% and 87% inhibition against SARS-CoV-2 M^{pro} when used in 100 and 10 μM, respectively with an IC$_{50}$ of 0.94 and 1.18 μM against SARS-CoV-2 and SARS-CoV M^{pro}, respectively.[22] Thereby considering the ability of the proposed compounds **I–X** to interact with the SARS-CoV-2 M^{pro} binding site with higher binding score and/or number of residues interaction using two different X-ray crystals might open the way to discover a potent antiviral M^{pro} inhibitor.

It was noticed that the best computational outcome of **I–X** were the coumarin containing scaffold **II–VI**. The mentioned compounds showed binding energy scores of −6.56, −6.31, −5.99, −5.94 and −5.82 kcal mol^{-1} for **VI**, **V**, **III**, **IV** and **II**, respectively which preceded the co-crystallized ligand 3WL that showed −5.77 kcal mol^{-1}. Moreover unlike 3WL; these compounds managed to interact with at least one of the two critical catalytic residues of M^{pro}, His 41 and Cys 145, as
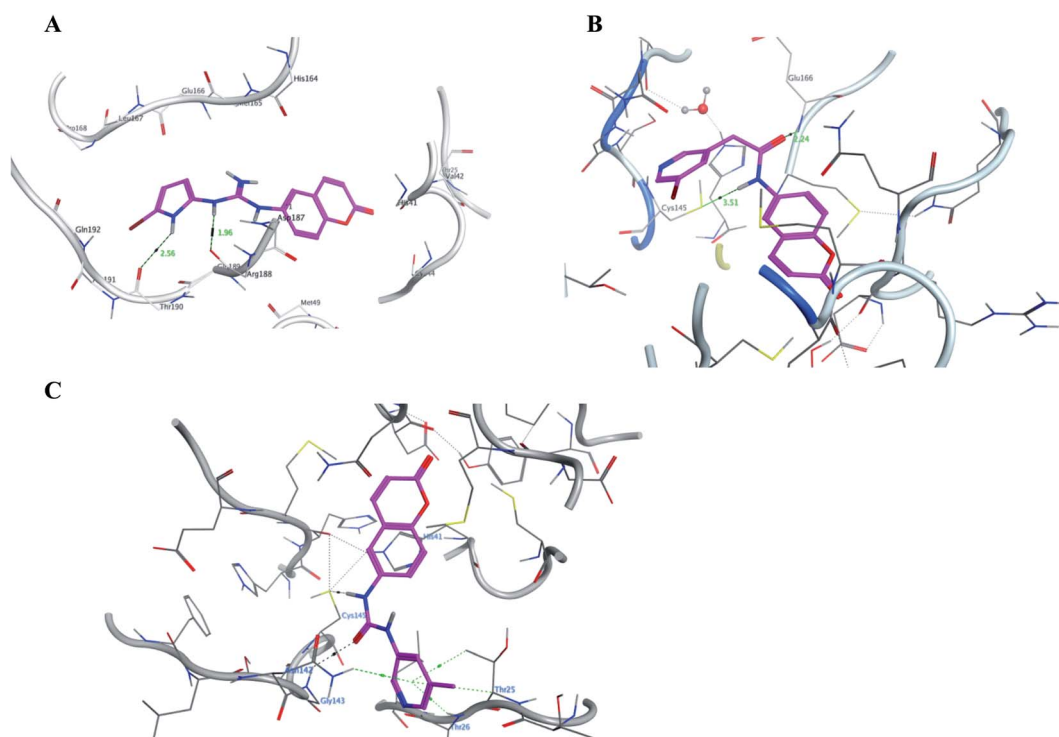

Fig. 17 A graphical interaction between **III**, **IV** and **VI** (in magenta sticks) and the crucial residues of 6M2N M^{pro} where (A) was **VI** showing two hydrogen bonds (black dotted line) with distance 1.56 and 2.56 Å, (B) was **III** forming two H bonds (black dotted lines) with distance 2.24 and 3.51 Å, and (C) was **IV** forming many bonds (green and black dotted lines).
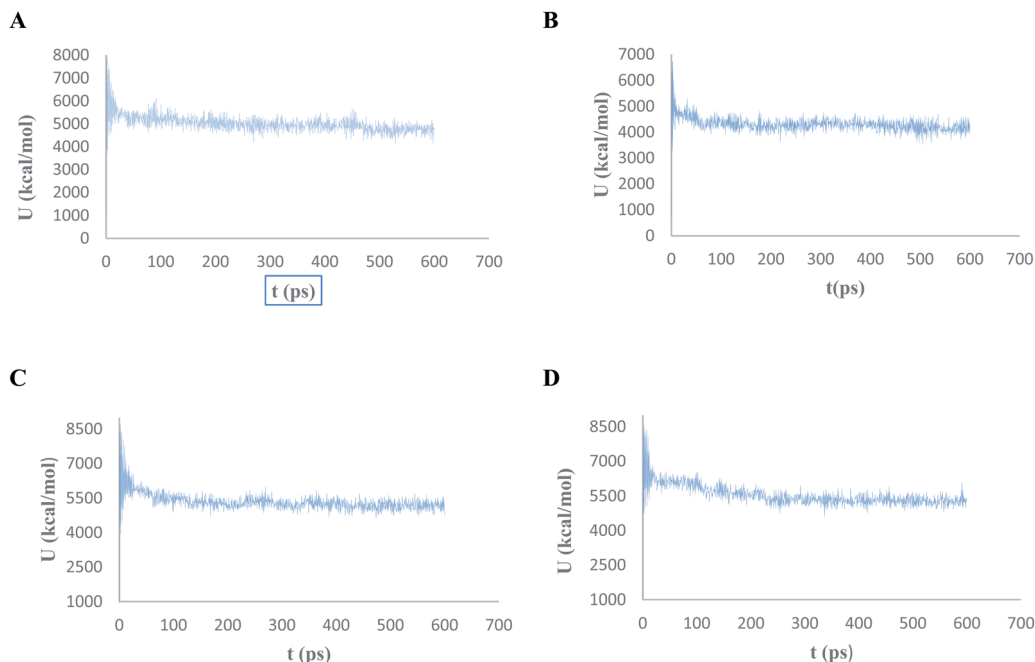
Fig. 18 The evaluation of potential energy of complex of (A) compound **V**, (B) compound **VI**, (C) compound **IV**, and (D) compound **III** with PDB: 6M2N receptor site as function of time.

declared in Table 1. The most promising compound **VI** bound by its coumarin scaffold to 6M2N His 41 through arene–arene interaction while acted as H- bond donor to engage with both Arg 188 and Thr 190 through guanine –NH linkage and pyrrole –NH, respectively. On the other hand, it succeeded to bind to both 6Y2E catalytic residues through two arene–cation linkages and two H-bonds interactions with His 41 and Cys 145, respectively. Likewise, the second promising compound **V** bound through its coumarin scaffold to His 41 by arene–arene bond and to Cys 145 and Asn 142 through H-bond in 6M2N and 6Y2E, respectively. In a similar manner, compound **III** served as H-bond donor *via* its amide –NH to anchor Cys 145 in both 6M2N and 6Y2E. However; it managed to form another H-bond with 6M2N Glu 166, the essential residue for M^{pro} dimerization, through its amide carbonyl. Interestingly; out of the ten compounds, compound **IV** showed the highest number of

interactions with M^{pro} crucial residues in both PDB: 6M2N and 6Y2E with binding energy score −5.94 and −5.66 kcal mol^{-1}, respectively which indeed surpassed 3WL score and contact with M^{pro} binding site. The graphical representation of **III**, **IV** and **VI** interaction with the 6M2N M^{pro} substrate binding site is shown in Fig. 17.

Even though compounds **II–IV** and **V–VII** shared close chemical structure, yet changing few chemical groups altered their binding scores in different ways. Considering their chemical structures, the addition of a bromide group to the pyridine ring of **II** or changing its amide linkage to urea in both **III** and **IV**, respectively caused a mild improvement of its score value from −5.82 to −5.99 and −5.94 kcal mol^{-1}, respectively. In the same aspect; changing the methoxy group of **V** to a bromide in **VI** resulted in a moderate enhancement of its binding energy score value from −6.31 to −6.56 kcal mol^{-1},

Table 2 The physicochemical properties of **I–X** as calculated from MOE® 2020

#	lip_acc	lip_don	lip_drug like	log $P_{(o/w)}$	Weight (dalton)	lip_violation	opr_nrot	TPSA (Å^2)	Mutagen groups
I	5.00	0.00	1.00	3.79	324.16	0.00	2.00	57.01	0.00
II	5.00	1.00	1.00	2.35	294.31	0.00	3.00	68.29	0.00
III	7.00	4.00	1.00	3.40	298.30	0.00	5.00	99.23	0.00
IV	5.00	4.00	1.00	2.53	251.29	0.00	4.00	76.59	0.00
V	5.00	4.00	1.00	3.37	330.19	0.00	4.00	76.59	0.00
VI	5.00	4.00	1.00	2.34	280.13	0.00	4.00	76.59	0.00
VII	7.00	6.00	1.00	2.93	285.28	1.00	4.00	111.97	0.00
VIII	6.00	5.00	1.00	4.03	348.74	0.00	4.00	91.74	0.00
IX	6.00	1.00	1.00	1.90	295.29	0.00	2.00	80.32	0.00
X	5.00	1.00	1.00	2.85	359.18	0.00	3.00	68.29	0.00

Table 3 The pharmacokinetics properties of compounds **I–X** as calculated by SwissADME®

#	GI absorption	BBB permeability	*P*-glycoprotein substrate	Inhibitor of CYP P450
I	High	No	No	Yes
II	High	Yes	No	Yes
III	High	Yes	No	Yes
IV	High	No	No	No except CYP 1A2
V	High	No	No	No except CYP 1A2
VI	High	No	No	No except CYP 1A2
VII	High	No	No	No except CYP 1A2
VIII	High	Yes	Yes	No except CYP 1A2, 2D6
IX	High	Yes	Yes	Yes
X	High	Yes	No	No except CYP 1A2

respectively. However, changing the methoxy group of **V** to a hydroxyl group in **VII** dropped its binding score from −6.31 to −5.75 kcal mol⁻¹, respectively.

Regarding the other four compounds **I** and **VIII–X**; despite displaying less score values than 3WL in 6M2N, they showed appreciated number of interactions with the crucial residues in the catalytic center and substrate binding site in both 6M2N and 6Y2E unlike 3WL as explained earlier. Moreover, those compounds showed better binding energy score values in molecular docking using 6Y2E than 3WL as previously stated in Table 1.

4.6. Molecular dynamics simulation

The conformational flexibilities of the proposed docked compounds with the M^pro enzyme were examined *via* MD process to attain dependable drug receptor – binding affinities. MD process calculations were run for 600 ps on the most promising compounds **III–VI** to target M^pro enzyme (PDB: 6M2N). Fig. 18 showed the results of the atomic potential energy function (U) during dynamic study calculation for the proposed compounds **III–VI** in the 6M2N at its binding site. To explore the dynamic stability of the 6M2N/inhibitor drugs complexes, the time-dependent potential energy of the complex were calculated during MD trajectories. It was apparent in Fig. 18, that complex (A) (6M2N/compound **V**) achieved equilibrium around 400 ps. Meanwhile complex (B) (6M2N/compound **VI**) achieved the equilibrium around 300 ps. On the other hand, complex (C) and complex (D) (6M2N/compound **IV** and **III**, respectively) achieved the equilibrium stability around 400 ps.

4.7. *In silico* physicochemical, drug likeliness and pharmacokinetics evaluation

4.7.1. Physicochemical, drug likeliness and mutagenicity.
In order to assess the drug-likeliness properties of **I–X**; their physicochemical characters were evaluated considering Lipinski's, Veber's rules and the presence of mutation groups using MOE® 2020 and SwissADME® website.[36] Lipinski's rule dictates that the compound is orally bioavailable if it has a molecular weight less than 500 daltons, no more than 5 H-bond donor, less than 10 H-bond acceptor groups and log *P* should not exceed 5.[37] While Veber's declared that the compound to be accepted as drug potential should have no more than 10

rotatable bonds and its topological polar surface area should not exceed 120 Å to pass through the cell membrane.[38,39]

The calculated physicochemical properties of **I–X** were shown in Table 2 stating no violation and full compliance to both drug-likeliness rules except for **VII** that had six H-bond donor groups. However, **VII** is still considered as a good theoretical drug candidate as explained by Lipinski's. Moreover all compounds **I–X** had bioavailability score of 0.55 and complied Ghose's, Egan's and Mugge's rules of drug likeness as calculated from SwissADME®.

On the other hand, **I–X** displayed the complete absence of any possible mutagenic groups consequently; they could be submitted for further chemical and biological *in vitro* investigation as the second phase.

4.7.2. Pharmacokinetic properties.
Upon calculating the pharmacokinetic properties of **I–X**, SwissADME® had revealed the following data shown in Table 3 based on their chemical structures. All compounds were foreseen to have high gastric absorption that complied with the stated bioavailability score. Nonetheless; **II**, **III** and **VIII–X** were expected to pass the blood brain barrier (BBB) which might cause CNS side effects in generalized treatment. On the other hand, these BBB permeable compounds might be beneficial to treat some of the neurological disorders SARS family causes thus, needs further *in vitro* investigation to evaluate their actual degree of BBB permeability and their CNS therapeutic effect.

Additionally; SwissADME® could also predict the possibility of the compounds to be affected by *P*-glycoprotein, a cellular efflux pump that pumps out drugs to extracellular fluid, where only **VIII** and **IX** were predicted to be substrate for it that might affect their plasma concentration and biological effect. Moreover; cytochrome P450 (CYP P450) enzymes family might be affected with different degrees by **I–X** as assumed according to their chemical structures that detailed in Table 3.

The top docking scored **V** and **VI** were presumed to be neither BBB permeable nor susceptible to *P*-glycoprotein. In addition, they expectedly did not inhibit CYP family expect CYP1A2 that might be affected to certain degree.

5. Conclusion

The most influential finding to emerge from this work was that compounds **I–X** revealed good molecular docking results

compared with baicalein **8** in terms of binding energy scores and their interactions with the crucial amino acids of SARS-CoV-2 M^{pro} binding site. The best *in silico* outcome was achieved by derivatives **V** and **VI** regarding the pharmacophore RMSD, docking scores to SARS-CoV-2 M^{pro} PDB files and molecular dynamic simulation. Both **V** and **VI** showed better binding scores *versus* the crystallized ligand **8** giving −6.31, −6.56 and −5.77 kcal mol^{-1}, respectively. They matched the calculated pharmacophore model with RMSD 0.43 and 0.57 for **V** and **VI**, respectively. Also, the mentioned compounds showed encouraging binding affinity to M^{pro} enzyme and good compliance with both Lipinisk's and Veber's rules. Further investigation and experimentation to these derivatives is highly recommended which may become promising candidates for COVID-19 therapy.

Contributors

NMM initiated and developed the scope of the study with conceptualization, formal analysis, project administration, methodology in molecular docking and ADMET data generation and analysis. EMHA contributed with the protein alignment and pharmacophore generation part of the study with their corresponding data analysis and figures elucidation. AMA designed the molecular dynamics study with its corresponding data analysis and figures elucidation. All authors contributed jointly with the manuscript original draft writing where NMM generated the final revised manuscript that was read and approved by the other authors.

Conflicts of interests

We declare that we have no conflicts of interest.

Acknowledgements

References

1 W. H. Organization, *WHO Coronavirus Disease (COVID-19) Dashboard*, https://covid19.who.int/?gclid=Cj0KCQjw-O35BRD VARIsAJU5mQWekRZOAT2nMi7M_-aCZ0knit3e5R3pblHmDIUZ_W8OtC1oGSnDjOEaApjZEALw_wcB, accessed 22 October 2020.

2 A. Wu, Y. Peng and B. Huang, Genome Composition and Divergence of the Novel Coronavirus (2019-nCoV) Originating in China, *Cell Host Microbe*, 2020, **27**, 325–328.

3 F. Giorgi and C. Ceraolo, Genomic Variance of the 2019-nCoV Coronavirus, *J. Med. Virol.*, 2020, **92**(5), 522–528.

4 F. Organization, *FDA Approves First Treatment for COVID-19*, https://www.fda.gov/news-events/press-announcements/fda-approves-first-treatment-covid-19, accessed 31 October 2020.

5 F. Organization, *Fact Sheet for Healthcare Providers Emergency Use Authorization (EUA) of Veklury® (Remdesivir) for Hospitalized Pediatric Patients Weighing 3.5 kg to Less Than 40 kg or Hospitalized Pediatric Patients Less Than 12 Years of Age Weighing at Least 3.5 kg*, https://www.fda.gov/media/137566/download, accessed 01 Nov. 2020.

6 P. C. Y. Woo, Y. Huang, S. K. P. Lau and K.-Y. Yuen, Coronavirus Genomics and Bioinformatics Analysis, *Viruses*, 2010, **2**, 1804–1820.

7 A. Wu, Y. Peng and B. Huang, Genome Composition and Divergence of the Novel Coronavirus (2019-nCoV) Originating in China, *Cell Host Microbe*, 2020, **27**, 325–328.

8 J. Ziebuhr, E. J. Snijder and A. E. Gorbalenya, Virus-Encoded Proteinases and Proteolytic Processing in the Nidovirales, *J. Gen. Virol.*, 2000, **81**(4), 853–879.

9 J. Zeibuhr and A. Hegyi, Conservation of Substrate Specificities among Coronavirus Main Proteases, *J. Gen. Virol.*, 2002, **83**(3), 595–599.

10 K. Anand, J. Ziebuhr, P. Wadhwani, J. R. Mesters and R. Hilgenfeld, Coronavirus Main Proteinase (3CL^{Pro}) Structure: Basis for Design of Anti-Sars Drugs, *Science*, 2003, **300**(5626), 1763–1767.

11 J. Zeibuhr, Molecular Biology of Severe Acute Respiratory Syndrome Coronavirus, *Curr. Opin. Microbiol.*, 2004, **7**(4), 412–419.

12 K. Ś. A. V. Moliner, Revealing the Molecular Mechanisms of Proteolysis of SARS-CoV-2 M^{pro} by Qm/Mm Computational Methods, *Chem. Sci.*, 2020, **11**(39), 10626–10630.

13 B. G. A. D. Goyal, Targeting the Dimerization of the Main Protease of Coronaviruses: A Potential Broad-Spectrum Therapeutic Strategy, *ACS Comb. Sci.*, 2020, **22**(6), 297–305.

14 L. Zhang, D. Lin and X. Sun, Crystal Structure of SARS-CoV-2 Main Protease Provides a Basis for Design of Improved A-Ketoamide Inhibitors, *Science*, 2020, **368**, 409–412.

15 U. Bacha, J. Barrila and A. Velazquez-Campoy, Identification of Novel Inhibitors of the SARS Coronavirus Main Protease 3CL^{Pro}, *Biochemistry*, 2004, **43**, 4906–4912.

16 L. Lu, N. Mahindroo and P. Liang, Structure-Based Drug Design and Structural Biology Study of Novel Nonpeptide Inhibitors of Severe Acute Respiratory Syndrome Coronavirus Main Protease, *J. Med. Chem.*, 2006, **49**(17), 5154–5161.

17 N. Z. Zhong and S. Zou, Without Its N-Finger, the Main Protease of Severe Acute Respiratory Syndrome Coronavirus Can Form a Novel Dimer through Its C-Terminal Domain, *J. Virol.*, 2008, **82**, 4227–4234.

18 J. S. L. Lim, Y. Mu and J. Song, Dynamically-Driven Enhancement of the Catalytic Machinery of the SARS 3C-Like Protease by the S284–T285-I286/a Mutations on the Extra Domain, *PLoS One*, 2014, **9**(7), e101941.

19 M. Stoermer, Homology Models of Coronavirus 2019-Ncov 3CL^{pro} Protease, *ChemRxiv*, 2020, DOI: 10.26434/chemrxiv.11637294.v3.

20 J. S. Morse, T. Lalonde, S. Xu and W. R. Liu, Learning from the Past: Possible Urgent Prevention and Treatment Options for Severe Acute Respiratory Infections Caused by 2019-nCoV, *ChemBioChem*, 2020, **21**, 730–738.

21 O. Sekiou, B. Ismail, B. Zihad and D. Abdelhak, *In Silico Identification of Potent Inhibitors of COVID-19 Main Protease (M^pro) and Angiotensin Converting Enzyme 2 (ACE-2) from Natural Products: Quercetin, Hispidulin, and Cirsimaritin Exhibited Better Potential Inhibition Than Hydroxy-Chloroquine against COVID-19 Main Protease Active Site and ACE-2*, 2020.

22 H. Su, S. Yao and W. Zhao, Anti-SARS-CoV-2 Activities *in vitro* of Shuanghuanglian Preparations and Bioactive Ingredients, *Acta Pharmacol. Sin.*, 2020, 1–11.

23 A. S.-H. J. Thanigaimalai Pillaiyar, An Overview of Severe Acute Respiratory Syndrome–Coronavirus (SARS-CoV) 3CL Protease Inhibitors: Peptidomimetics and Small Molecule Chemotherapy, *J. Med. Chem.*, 2016, **59**, 6595–6628.

24 K. Pumpor, S. Anemüller and K. Verschueren, A Structural View of the Inactivation of the SARS Coronavirus Main Proteinase by Benzotriazole Esters, *Chem. Biol.*, 2008, **15**, 597–606.

25 J. Yin, J. Zhang and C. Niu, Molecular Docking Identifies the Binding of 3-Chloropyridine Moieties Specifically to the S1 Pocket of SARS-CoV M^pro, *Bioorg. Med. Chem.*, 2008, **16**, 293–302.

26 K. King, C. Kuo and C. Wu, Stable Benzotriazole Esters as Mechanism-Based Inactivators of the Severe Acute Respiratory Syndrome 3CL Protease, *Chem. Biol.*, 2006, **13**, 261–268.

27 L. Eltis, H. Pettersson and J. Zhang, Design, Synthesis, and Evaluation of Inhibitors for Severe Acute Respiratory Syndrome 3C-Like Protease Based on Phthalhydrazide Ketones or Heteroaromatic Esters, *J. Med. Chem.*, 2007, **50**, 1850–1864.

28 N. Yasuo, M. Sekijima and R. Yoshino, Identification of Key Interactions between SARS-CoV-2 Main Protease and Inhibitor Drug Candidates, *Sci. Rep.*, 2020, **10**, 12493.

29 T. Giorgino, G. Fabritiis and I. Buch, Complete Reconstruction of an Enzyme-Inhibitor Binding Process by Molecular Dynamics Simulations, *Proc. Natl. Acad. Sci. U. S. A.*, 2011, **108**, 10184–10189.

30 Y. E. A. Shan, How Does a Drug Molecule Find Its Target Binding Site, *J. Am. Chem. Soc.*, 2011, **133**, 9181–9183.

31 S. B. Needleman and C. D. Wunsch, A General Method Applicable to the Search for Similarities in the Amino Acid Sequences of Two Proteins, *J. Mol. Biol.*, 1970, **48**, 443–453.

32 J. B. Sturgeon and B. B. Laird, Symplectic Algorithm for Constant pressure Molecular Dynamics Using a Nos_E-Poincar_E Thermostat, *J. Chem. Phys.*, 2000, **112**(8), 3474–3482.

33 B. Goyal and D. Goyal, Targeting the Dimerization of the Main Protease of Coronaviruses: A Potential Broad-Spectrum Therapeutic Strategy, *ACS Comb. Sci.*, 2020, **22**(6), 297–305.

34 H. Pettersson, C. Huitema and J. Zhange, Design, Synthesis, and Evaluation of Inhibitors for Severe Acute Respiratory Syndrome 3C-Like Protease Based on Phthalhydrazide Ketones or Heteroaromatic Esters, *J. Med. Chem.*, 2007, **50**(8), 1850–1864.

35 Y. Wang, Y. Lin and L. Chen, Synthesis and Evaluation of Isatin Derivatives as Effective SARS Coronavirus 3CL Protease Inhibitors, *Bioorg. Med. Chem. Lett.*, 2005, **15**(12), 3058–3062.

36 A. Daina, O. Michielin and V. Zoete, SwissADME: A Free Web Tool to Evaluate Pharmacokinetics, Drug-Likeness and Medicinal Chemistry Friendliness of Small Molecules, *Sci. Rep.*, 2017, **7**, 42717.

37 C. Lipinski, Lead- and Drug Like Compounds: The Rule of Five Revolution, *Drug Discovery Today: Technol.*, 2004, **1**, 337–341.

38 S. J. D. Veber and H. Cheng, Molecular Properties That Influence the Oral Bioavailability of Drug Candidates, *J. Med. Chem.*, 2002, **45**(12), 2615–2623.

39 J. Kelder, Polar Molecular Surface as a Dominating Determinant for Oral Absorption and Brain Penetration of Drugs, *Pharm. Res.*, 1999, **16**(10), 1514–1519.